nature nanotechnology

LETTERS

PUBLISHED ONLINE: 28 JULY 2013 | DOI: 10.1038/NNANO.2013.140

A valley–spin qubit in a carbon nanotube

E. A. Laird†, F. Pei and L. P. Kouwenhoven*

Although electron spins in III–V semiconductor quantum dots have shown great promise as qubits[1–3], hyperfine decoherence remains a major challenge in these materials. Group IV semiconductors possess dominant nuclear species that are spinless, allowing qubit coherence times[4–6] up to 2 s. In carbon nanotubes, where the spin–orbit interaction allows for all-electrical qubit manipulation[7–10], theoretical predictions of the coherence time vary by at least six orders of magnitude and range up to 10 s or more[11,12]. Here, we realize a qubit encoded in two nanotube valley–spin states, with coherent manipulation via electrically driven spin resonance[2,3] mediated by a bend in the nanotube. Readout uses Pauli blockade leakage current through a double quantum dot[13–15]. Arbitrary qubit rotations are demonstrated and the coherence time is measured for the first time via Hahn echo, allowing comparison with theoretical predictions. The coherence time is found to be ∼65 ns, probably limited by electrical noise. This shows that, even with low nuclear spin abundance, coherence can be strongly degraded if the qubit states are coupled to electric fields.

The qubit operating principle[8] (Fig. 1a,b) relies on the existence of the valley degree of freedom, which classifies electron states according to the orbital angular momentum around the nanotube[16]. Spin ($\downarrow$,$\uparrow$) and valley (K,K') together lead to four states, separated by spin–orbit coupling[7,11,17–19] into doublets denoted $\{\Uparrow,\Downarrow\}$ and $\{\Uparrow^*,\Downarrow^*\}$. Both degrees of freedom have associated magnetic moments, with the valley moment much larger than the spin moment because of the comparatively large current loop of the circulating electron. The resulting single-particle spectrum is plotted in Fig. 1a as a function of magnetic field $\mathbf{B}$ directed parallel ($B_\parallel$) or perpendicular ($B_\perp$) to the nanotube axis. Whereas $B_\parallel$ couples to both spin and orbital moments, $B_\perp$ couples only via spin, so the energy splitting within each doublet depends on field direction. This is parameterized by an anisotropic effective $\mathbf{g}$-tensor with components $g_\parallel$ for parallel and $g_\perp < g_\parallel$ for a perpendicular field. Although for large $B_\parallel$ the four states $\{\Uparrow,\Downarrow,\Uparrow^*,\Downarrow^*\}$ take the simple forms on the right of Fig. 1a, in general they are entangled combinations of spin and valley eigenstates. Either doublet can act as a qubit, depending on the quantum dot occupation.

Qubit manipulation using an electric field is possible if the nanotube contains a bend (Fig. 1b)[8]. To understand this, consider each doublet as an effective spin-1/2. The anisotropic energy splitting is then equivalent to isotropic Zeeman coupling with g-factor $g_s = 2$, but with $\mathbf{B}$ replaced by a tilted effective magnetic field $\mathbf{B}_{\mathrm{eff}} = \mathbf{g} \otimes \mathbf{B}/g_s$. Where the nanotube is perpendicular to $\mathbf{B}$ (right side of Fig. 1b), $\mathbf{B}_{\mathrm{eff}}$ and $\mathbf{B}$ are parallel. However, where the angle is smaller (Fig. 1b, left), components $B_\parallel$ and $B_\perp$ contribute differently to $\mathbf{B}_{\mathrm{eff}}$, tilting $\mathbf{B}_{\mathrm{eff}}$ away from $\mathbf{B}$. Under application of an a.c. electric field, an electron driven across the bend experiences $\mathbf{B}_{\mathrm{eff}}$ to oscillate in direction. With the driving frequency set to $f = \Delta E/h$, where $\Delta E = g_s \mu_B |\mathbf{B}_{\mathrm{eff}}|$ is the qubit energy splitting, h is Planck's constant and μ_B is the Bohr magneton, this drives resonant transitions between qubit states, permitting arbitrary coherent single-qubit operations. Because the two qubit states do not have the same spin, driving transitions between them in this way leads to electrically driven spin resonance (EDSR).

As in previous experiments[1], the qubit is realized in a double quantum dot where it is initialized and read out by exploiting Pauli blockade. The device (Fig. 1c) consists of a single electrically contacted nanotube, which is bent by touching the substrate (Fig. 1d)[15]. The electrical potential is controlled using voltages applied to nearby gate electrodes, and tuned to configure the double dot close to the $(1,-1) \rightarrow (0,0)$ transition. Negative (positive) numbers in brackets denote electron (hole) occupations of left and right dots[20].

Figure 1e shows the current for 5 mV source–drain bias, measured as a function of gate voltages coupled to the left and right quantum dots without pulses or microwaves. The dashed quadrilateral outlines the gate space region where Pauli blockade strongly suppresses the current, with the corresponding valley–spin energy levels shown in the first panel of Fig. 1f. Although tunnelling through the double dot is energetically allowed, it is suppressed by valley–spin selection rules[15] because an electron loaded from the left in state $\Uparrow$ or $\Downarrow$ is forbidden by Pauli exclusion from entering the corresponding filled state on the right. Pauli blockade is broken by tunnelling events that do not conserve spin and valley, for example due to spin–orbit coupling combined with disorder[15,21], which give rise to leakage current near the triangle tips in Fig. 1e. Transport occurs by electrons in states $\{\Uparrow,\Downarrow\}$ on the left tunnelling into unoccupied $\{\Uparrow^*,\Downarrow^*\}$ states on the right.

The combined two-qubit state is defined by the states of the unpaired electrons in the left and right dots. Although Pauli blockade applies for any combination of $\{\Uparrow,\Downarrow\}$ on the left and $\{\Uparrow^*,\Downarrow^*\}$ on the right, the rate at which it is broken by disorder-induced valley mixing is different for different states because they contain different superpositions of valley–spin quantum numbers (see Supplementary Section SIII)[15,22]. The leakage current is therefore sensitive to the rate at which qubits are flipped.

To detect EDSR, the current is measured with the following cycle of pulses and microwave bursts applied to the gates (Fig. 1f)[1]. Beginning with the double dot configured inside the quadrilateral marked in Fig. 1e initializes a long-lived blocked two-qubit state, for example $\Downarrow\Downarrow^*$. The device is then pulsed along the detuning axis defined in Fig. 1e to a configuration in $(1,-1)$, following which the qubits are manipulated by applying microwaves for a time t_{burst}. If microwaves are resonant with either qubit, this will drive coherent rotation in at least one of the quantum dots, leading to a state such as $\Uparrow\Downarrow^*$. For readout, the device is returned to the Pauli blockade configuration, and if a qubit flip has occurred in either dot, so that the device is no longer in a long-lived state, an electron tunnels out into the right lead. Averaged over many cycles, the current is proportional to the qubit flip probability during the manipulation stage.

The measured EDSR spectrum is shown in Fig. 2 as a function of B_x, B_z, field angle θ in the x–z plane, and detuning (coordinates are defined in Fig. 1d). In each plot, EDSR is evident as an increased current at the resonance frequency, which depends on magnetic field. The spectrum is much more complex than previously measured

Kavli Institute of Nanoscience, Delft University of Technology, 2600 GA, Delft, The Netherlands, †Present address: Department of Materials, Oxford University, Oxford OX1 3PH, UK. *e-mail: L.P.Kouwenhoven@tudelft.nl

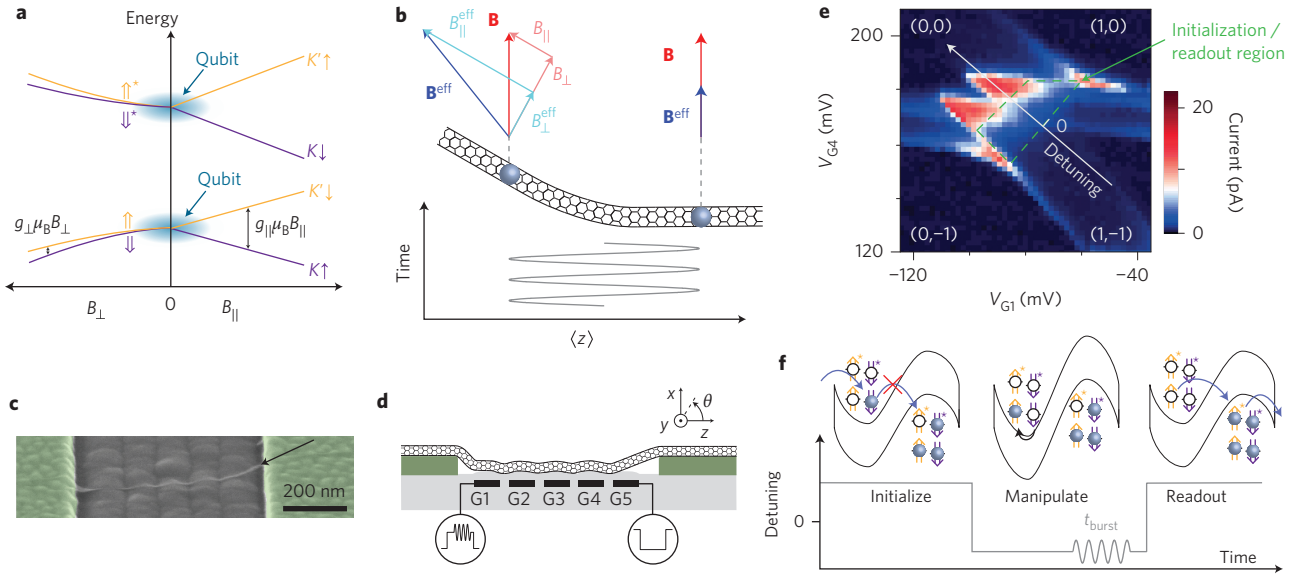

Figure 1 | Valley–spin resonance in a bent nanotube. a, Single-particle energy levels of a straight nanotube, as a function of parallel and perpendicular magnetic field. The two doublets are split with effective *g*-factors depending on the field orientation. Either doublet can act as a qubit. For large $B_\parallel$, the four states take the simple forms labelled on the right. **b**, Using a bend to mediate spin resonance. On the right, the nanotube is oriented perpendicular to **B** and therefore also to $\mathbf{B}^{eff}$. However, on the left, $\mathbf{B}^{eff}$ is a sum of parallel ($B^{eff}_\parallel$) and perpendicular ($B^{eff}_\perp$) components, which are related to $B_\parallel$ and $B_\perp$ by different components of the **g**-tensor. An electron driven back and forth experiences $\mathbf{B}^{eff}$ to vary periodically in direction, leading to spin resonance. **c**,**d**, Scanning electron microscopy image (**c**) and schematic (**d**) of the measured device. The bent nanotube (marked by the arrow) spans a trench between source and drain contacts (green). The electrical potential is controlled using voltages applied to gates G1–G5. **e**, Current through the device as a function of gate voltages on G1 and G4 close to the (1,−1) → (0,0) transition. Double-dot occupations in the four adjoining regions of gate space are indicated, and the detuning axis is marked by a light grey arrow. Inside the green quadrilateral, Pauli blockade makes the current sensitive to the valley–spin state. **f**, Cycle of gate voltage pulses for qubit manipulation and detection of EDSR.

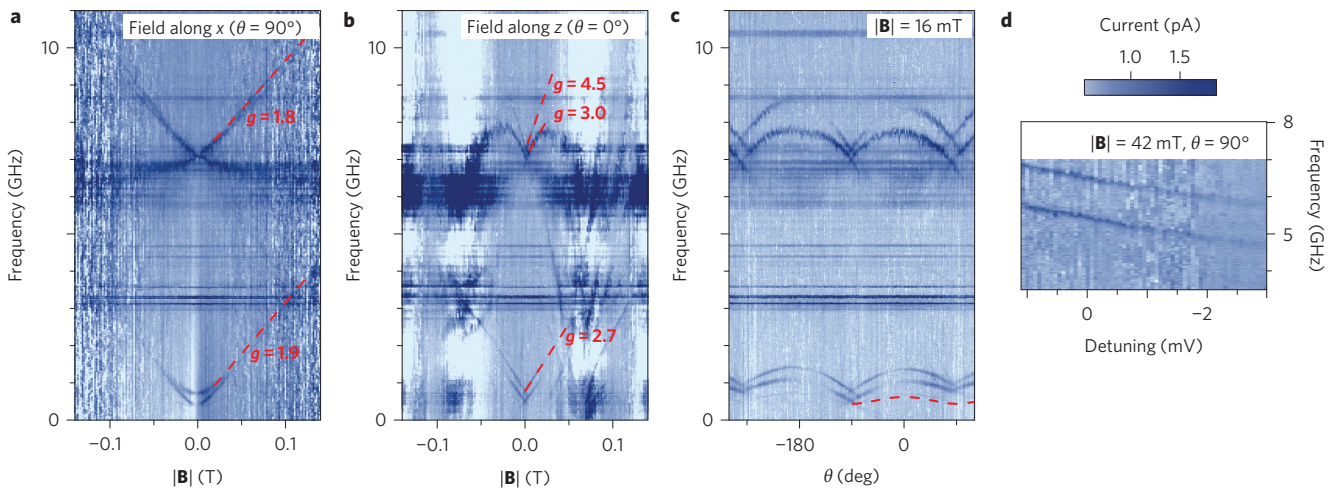

Figure 2 | Spin resonance spectroscopy. a–d, Average current with the pulse cycle of Fig. 1f applied, measured as a function of microwave frequency and magnetic field along the *x*-axis (**a**) and *z*-axis (**b**), magnetic field angle relative to the *z*-axis (**c**), and detuning during the manipulation pulse (**d**). Measured *g*-factors for selected resonance lines are indicated in **a** and **b**. Taking perpendicular and parallel *g*-factors for the lowest resonance predicts[8] the expected resonance frequency marked in **c**, which does not agree well with the observed spectrum. To make the signal clearer, a frequency-independent background has been subtracted from all four plots. The data in **d** were taken for slightly different device tuning than in **a**–**c**. Horizontal features reflect electrical resonances of the cryostat.

for spin qubits[1] or expected from the level diagram in Fig. 1a, but nevertheless shows some features that agree with theory[8]. At low frequency (between ~0.8 GHz and ~4 GHz), the spectrum exhibits an approximately linear increase of resonance frequency with |**B**| (Fig. 2a,b), with *g*-factors (dashed lines in Fig. 2a,b) higher along *z* than along *x*, indicating coupling to the valley degree of freedom. However, the anisotropy is much less than expected from Coulomb blockade spectroscopy, which yields *g*-factors larger along *z* and smaller along *x* (Supplementary Section SII). Furthermore, the angular dependence of the spectrum (dashed line in Fig. 2c) agrees only qualitatively with that expected[8] from the measured *g*-factors. This reflects the fact that the resonance lines in Fig. 2a,b do not extrapolate to zero, with the extrapolated zero-field resonance being higher for the lines in Fig. 2b.

A qualitatively unexpected feature is the pronounced series of resonances centred around 7 GHz. Such a high-frequency manifold

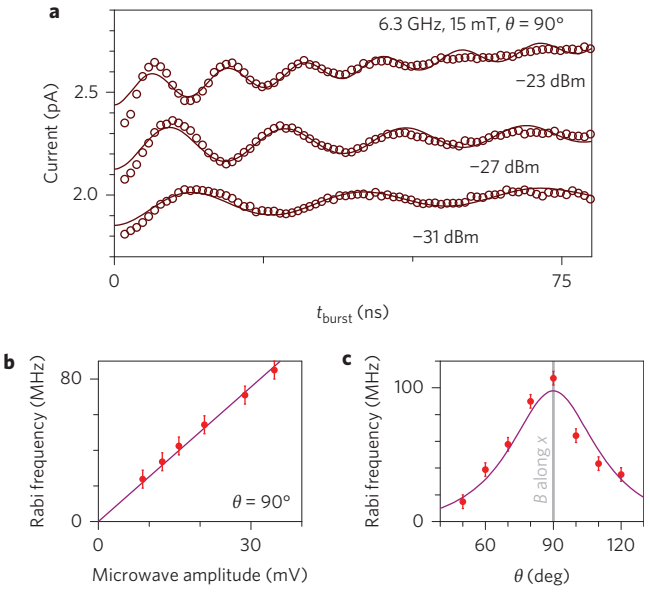

Figure 3 | Coherent qubit manipulation a, Points: current as a function of t_{burst} measured on the highest resonance, for three different values of the microwave power at the sample holder. Rabi oscillations show coherent control of the qubit. Lines: fits to damped oscillations, appropriate for a driven qubit undergoing quasi-static dephasing (Supplementary Section SIV)[23]. Middle and upper traces are offset for clarity. (The device tuning changed slightly between Figs 2 and 3, leading to a lower resonance frequency.) **b**, Rabi frequency (points), with error bars marking fit uncertainty as a function of root mean square microwave voltage at the sample holder. As expected, the data show good agreement with a linear fit, with a slope consistent with bent-nanotube EDSR (see Supplementary Section SV). **c**, Rabi frequency (points, with error bars marking fit uncertainty) as a function of field angle at constant microwave power and frequency, showing a maximum for field along the *x*-axis. The data agree well with a theoretical fit[8] (line) taking the *g*-factors measured on the topmost lines in Fig. 2a,b, and treating the overall scaling as a fit parameter.

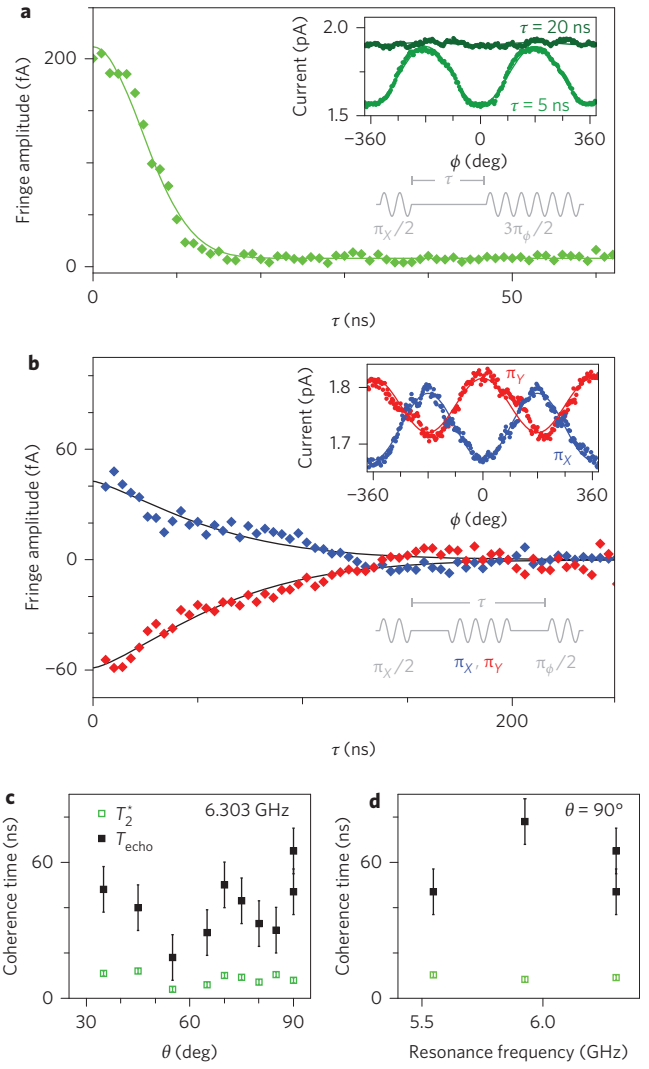

Figure 4 | Universal control and measurement of coherence times. **a**, Points: amplitude of Ramsey fringes, measured using a $\pi_x/2 - \tau - 3\pi_\phi/2$ microwave burst sequence (bottom inset) under the same conditions as Fig. 3a, plotted as a function of τ. Line: fit to Gaussian decay, giving $T_2^* = 8 \pm 1$ ns. Upper inset: current (points) as a function of microwave phase for two values of τ, together with cosinusoidal fits (lines). The observed fringes for $\tau = 5$ ns indicate that qubit rotations are achieved about arbitrary axes. **b**, Extending the coherence time via echo. Main panel shows fringe amplitude (points) in an echo pulse sequence as a function of τ, with the π pulse phase chosen along Bloch axes *X* (red) or *Y* (blue). Fits (lines) to a decay of the form $\exp(-(\tau/T_{echo})^\alpha)$ with $\alpha = 1.3 \pm 0.2$ give coherence time $T_{echo} = 65 \pm 10$ ns. Upper inset: current (points) as a function of $\pi/2$ phase for π phase along *x* and *y*, together with cosinusoidal fits (lines). As expected, the phase is reversed for π rotations about orthogonal axes. In both **a** and **b**, the lower inset shows a schematic of microwave burst sequence and definition of τ. **c**, Coherence times as a function of field angle, measured at constant resonance frequency and Rabi frequency (and therefore increasing drive power for decreasing θ). **d**, Coherence times as a function of resonance frequency, measured at constant Rabi frequency with field applied along *x*. Within experimental error (set by the estimated uncertainty in the fit parameters), no significant dependence on angle or frequency is seen.

could be expected from transitions between starred and unstarred states in Fig. 1a. However, the corresponding resonance frequency, set by the spin–orbit energy, would be ~200 GHz, far higher than measured. We suggest that the complex spectrum instead reflects inter-dot exchange[24], with the multiple bends in the nanotube induced by the surface, and possibly Rashba-type spin–orbit coupling[10]. The upper resonance is observed to shift as a function of detuning (Fig. 2d). We tentatively ascribe this to a change of exchange with detuning, although it could also be due to a shift of the electron wavefunction around a bend. In either case, this effect could be useful for bringing a qubit rapidly in and out of resonance using a detuning pulse. Although spin–orbit-mediated driving is expected[2,3,8] to become more efficient at higher $|\mathbf{B}|$, the corresponding increase in resonant current is not observed. This is probably because the background leakage current increases with field, making qubit initialization less efficient.

Coherent operation of the qubit is demonstrated in Fig. 3 by measuring the resonant current as a function of t_{burst}. The current is observed to oscillate (Fig. 3a) with a frequency proportional to the microwave driving amplitude (Fig. 3b). These Rabi oscillations arise from coherent precession of the qubit state during the burst. Although the data presented are for the highest-frequency resonance because it gave best contrast, Rabi oscillations were also observed for the other resonance lines in Fig. 2a.

Two other mechanisms have been proposed for coherent EDSR in nanotubes: Rashba-like spin–orbit coupling induced by the electric field of the gates[10,11], and coupling to spatially inhomogeneous disorder[9]. Measurement of Rabi frequency as a function of θ gives insight into the mechanism. As shown in Fig. 3c, the Rabi frequency at constant driving frequency and power is maximal for perpendicular $\mathbf{B}$. The dependence on angle agrees well with the bent nanotube prediction[8], taking the *g*-factors measured from Fig. 2a,b as fixed

and treating the overall coupling as a free parameter. In contrast, for Rashba-like coupling, the spin–orbit field in our geometry is predominantly along y, making the Rabi frequency nearly independent of field angle in the x–z plane[10]. For disorder-mediated EDSR, the angle dependence is unknown[9]. The data in Fig. 3 are therefore consistent with the bend being the main EDSR mechanism, although other effects probably contribute. Figure 2 provides evidence, in particular, of a Rashba-like contribution, in that the signal is evident even at at $|\mathbf{B}| = 0$ (Fig. 2a,b), where bend-mediated EDSR is predicted to be absent[8]. In contrast, the Rashba-like mechanism gives a finite signal even at zero field, as observed[10].

Rabi oscillations demonstrate qubit rotations about one axis of the Bloch sphere, but universal control requires rotations about two independent axes. This is demonstrated by a Ramsey fringe experiment, in which the single microwave burst of Fig. 1f is replaced by a pair of bursts inducing rotations by $\pi/2$ and $3\pi/2$ (Fig. 4a), with phase difference ϕ. With the first rotation taken as defining the Bloch X-axis, the second rotation acts around an axis offset by angle ϕ in the X–Y plane. As expected, the current oscillates as a function of ϕ depending on whether the two rotations interfere constructively or destructively (Fig. 4a, inset). As the burst interval τ is increased, the interference contrast decreases, yielding dephasing time $T_2^* = 8$ ns (Fig. 4a). Coherence can be prolonged by inserting a π burst to cancel slowly varying dephasing sources via Hahn echo (Fig. 4b). The decoherence time from the decay of fringes is then $T_{\mathrm{echo}} = 65$ ns. Further π bursts (Carr–Purcell decoupling) did not increase the coherence time. No signficant dependence of T_{echo} on field angle or magnitude was found (Fig. 4c,d).

The measured T_2^* is consistent with the hyperfine coupling measured previously in nanotube double dots, which may therefore be the dominant dephasing mechanism (alternatives are considered in Supplementary Section SVI)[1,13,14,25]. However, the short T_{echo} (compared with GaAs) is inconsistent with hyperfine decoherence, unless nuclear spin diffusion is extremely rapid[1]. We speculate that it is at least partly due to charge noise, which couples to the qubit because the resonance frequency depends on detuning (Fig. 2d). The gate voltage jitter implied by the measured decay (Supplementary Section SVI) is ~3.6 mV (including low-frequency noise) for T_2^* and ~0.6 mV (for broadband noise, but excluding low frequencies that are echoed away) for T_{echo}. Although we cannot exclude such a level of gate noise, it is more than ten times larger than the attenuated noise of the waveform generator ($\leq$0.05 mV). A more likely source of equivalent noise is charge switchers in the substrate. This work suggests ways to address both mechanisms. Fabricating nanotubes from isotopically purified ^{12}C feedstock[4] eliminates hyperfine decoherence, while charge noise can be reduced by fully suspending the nanotube and measuring at lower temperature[26].

Methods

The nanotube was grown using a chemical vapour deposition process known[27] to give a high yield of single-walled nanotubes with diameters of 1–3 nm. The device was previously measured in a separate cooldown described in ref. 15, and the fabrication is described there in detail. Measurements were performed at 270 mK in a ^{3}He refrigerator equipped with a vector magnet. Except for the scenario for Supplementary Fig. S1, the magnetic field was applied in the x–z plane defined in Fig. 1d, where the x-axis is normal to the chip and the z-axis runs perpendicular to the gates. Because the growth direction was uncontrolled, the nanotube was misaligned from this plane by ~6°. Schottky barriers with contact electrodes defined the left and right barriers of the double quantum dot, and the central barrier was defined by an n–p junction. From the curvature of charge transition lines in the stability diagram[28], the tunnel coupling was estimated as $t_c = 0.9 \pm 0.3$ meV. The double-dot occupancy was tuned using gate voltages and determined by identifying the bandgap in the charge stability diagram, with Pauli blockade recognized by a pronounced current suppression for one bias direction that was strongly affected by the magnetic field. The overall pulse cycle duration was typically 1 μs, split between a measurement pulse of ~400 ns and a manipulation pulse of ~600 ns.

Received 31 October 2012; accepted 18 June 2013; published online 28 July 2013

References

1. Hanson, R., Kouwenhoven, L. P., Petta, J. R., Tarucha, S. & Vandersypen, L. M. K. Spins in few-electron quantum dots. *Rev. Mod. Phys.* **79,** 1217–1265 (2007).
2. Nowack, K. C., Koppens, F. H. L., Nazarov, Y. V. & Vandersypen, L. M. K. Coherent control of a single electron spin with electric fields. *Science* **318,** 1430–1433 (2007).
3. Nadj-Perge, S., Frolov, S. M., Bakkers, E. P. A. M. & Kouwenhoven, L. P. Spin–orbit qubit in a semiconductor nanowire. *Nature* **468,** 1084–1087 (2010).
4. Balasubramanian, G. *et al.* Ultralong spin coherence time in isotopically engineered diamond. *Nature Mater.* **8,** 383–387 (2009).
5. Tyryshkin, A. M. *et al.* Electron spin coherence exceeding seconds in high-purity silicon. *Nature Mater.* **11,** 143–147 (2012).
6. Pla, J. J. *et al.* A single-atom electron spin qubit in silicon. *Nature* **489,** 541–545 (2012).
7. Kuemmeth, F., Ilani, S., Ralph, D. C. & McEuen, P. L. Coupling of spin and orbital motion of electrons in carbon nanotubes. *Nature* **452,** 448–452 (2008).
8. Flensberg, K. & Marcus, C. M. Bends in nanotubes allow electric spin control and coupling. *Phys. Rev. B* **81,** 195418 (2010).
9. Palyi, A. & Burkard, G. Disorder-mediated electron valley resonance in carbon nanotube quantum dots. *Phys. Rev. Lett.* **106,** 086801 (2011).
10. Klinovaja, J., Schmidt, M. J., Braunecker, B. & Loss, D. Carbon nanotubes in electric and magnetic fields. *Phys. Rev. B* **84,** 085452 (2011).
11. Bulaev, D. V., Trauzettel, B. & Loss, D. Spin–orbit interaction and anomalous spin relaxation in carbon nanotube quantum dots. *Phys. Rev. B* **77,** 235301 (2008).
12. Rudner, M. S. & Rashba, E. I. Spin relaxation due to deflection coupling in nanotube quantum dots. *Phys. Rev. B* **81,** 125426 (2010).
13. Churchill, H. O. H. *et al.* Electron–nuclear interaction in ^{13}C nanotube double quantum dots. *Nature Phys.* **5,** 321–326 (2009).
14. Churchill, H. O. H. *et al.* Relaxation and dephasing in a two-electron ^{13}C nanotube double quantum dot. *Phys. Rev. Lett.* **102,** 166802 (2009).
15. Pei, F., Laird, E. A. A., Steele, G. A. & Kouwenhoven, L. P. Valley–spin blockade and spin resonance in carbon nanotubes. *Nature Nanotech.* **7,** 630–634 (2012).
16. Minot, E. D., Yaish, Y., Sazonova, V. & McEuen, P. L. Determination of electron orbital magnetic moments in carbon nanotubes. *Nature* **428,** 536–539 (2004).
17. Jhang, S. H. *et al.* Spin–orbit interaction in chiral carbon nanotubes probed in pulsed magnetic fields. *Phys. Rev. B* **82,** 041404 (2010).
18. Jespersen, T. S. *et al.* Gate-dependent spin–orbit coupling in multielectron carbon nanotubes. *Nature Phys.* **7,** 348–353 (2011).
19. Wunsch, B. Few-electron physics in a nanotube quantum dot with spin–orbit coupling. *Phys. Rev. B* **79,** 235408 (2009).
20. Steele, G. A., Gotz, G. & Kouwenhoven, L. P. Tunable few-electron double quantum dots and Klein tunnelling in ultraclean carbon nanotubes. *Nature Nanotech.* **4,** 363–367 (2009).
21. Palyi, A. & Burkard, G. Spin–valley blockade in carbon nanotube double quantum dots. *Phys. Rev. B* **82,** 155424 (2010).
22. Reynoso, A. A. & Flensberg, K. Dephasing and hyperfine interaction in carbon nanotubes double quantum dots: disordered case. *Phys. Rev. B* **85,** 195441 (2012).
23. Koppens, F. H. L. *et al.* Universal phase shift and nonexponential decay of driven single-spin oscillations. *Phys. Rev. Lett.* **99,** 106803 (2007).
24. Nowak, M. P., Szafran, B. & Peeters, F. M. Resonant harmonic generation and collective spin rotations in electrically driven quantum dots. *Phys. Rev. B* **86,** 125428 (2012).
25. Reynoso, A. A. & Flensberg, K. Dephasing and hyperfine interaction in carbon nanotube double quantum dots: the clean limit. *Phys. Rev. B* **84,** 205449 (2011).
26. Dial, O. E., Shulman, M. D., Harvey, S. P. & Bluhm, H. Charge noise spectroscopy using coherent exchange oscillations in a singlet–triplet qubit. *Phys. Rev. Lett.* **110,** 146804 (2013).
27. Kong, J., Soh, H. T., Cassell, A. M., Quate, C. F. & Dai, H. J. Synthesis of individual single-walled carbon nanotubes on patterned silicon wafers. *Nature* **395,** 878–881 (1998).
28. Van der Wiel, W. G. *et al.* Electron transport through double quantum dots. *Rev. Mod. Phys.* **75,** 1–22 (2003).

Acknowledgements

The authors thank G.A. Steele, K. Flensberg, J. Klinovaja, D. Loss, A. Pályi, J. van den Berg, S.M. Frolov and V.S. Pribiag for discussions. This work was supported by the Netherlands Organization for Scientific Research (NWO)/the Dutch Organization for Fundamental Research on Matter (FOM).

Author contributions

F.P. fabricated and characterized the device. E.A.L. performed the experiment. All authors prepared the manuscript.

Additional information

Supplementary information is available in the online version of the paper. Reprints and permissions information is available online at www.nature.com/reprints. Correspondence and requests for materials should be addressed to L.P.K.

Competing financial interests

The authors declare no competing financial interests.

nature nanotechnology

SUPPLEMENTARY INFORMATION

DOI: 10.1038/NNANO.2013.140

Supplementary Information: A valley-spin qubit in a carbon nanotube

E. A. Laird,[1] F. Pei,[1] and L. P. Kouwenhoven[1]

[1]*Kavli Institute of Nanoscience, Delft University of Technology, 2600 GA, Delft, The Netherlands.*

Contents

I. LOCATION OF THE QUBIT

We exclude the possibility of parasitic EDSR, due to e.g. paramagnetic defects in the substrate or molecules adsorbed onto the nanotube, by the following evidence: (i) EDSR is not detected outside the Pauli blockade readout region shown in Fig. 1e, nor at other non-blockaded transitions. (ii) The anisotropy of the g-tensor is unlikely to originate from a strongly confined impurity spin, but is expected from the orbital moment of the nanotube. (iii) The symmetry of the spectrum as a function of angle in three dimensions is consistent with a principal axis aligned with the nanotube (Fig. S1). If defects in the substrate have any preferred axis, it would by symmetry be perpendicular to the chip, inconsistent with the data. (iv) EDSR was also observed in a similar device[1], whereas absorption of two paramagnetic impurities by different devices is unlikely. These arguments confirm that the measured qubit is located in the nanotube double quantum dot.

II. DC TRANSPORT MEASUREMENTS

A. Stability diagram

The full stability diagram is shown in Fig. S2. In these measurements, the nanotube bandgap can be identified, and therefore the absolute occupations of the double dot close to a particular transition is known. Surprisingly, the spacing of Coulomb peaks on either side of the bandgap is only ~ 1.5 times larger than the regular peak spacing, implying a bandgap of only ~ 10 meV (as opposed to ~ 30 meV measured in a previous cooldown[1]). (This could reflect a change in strain in the device[3] or a coating of dielectric, for example condensed water, modifying electron-electron interactions.[4]) Nevertheless, we believe the data in Fig. S2 securely identify the measured transition as (1,-1) - (0,0).

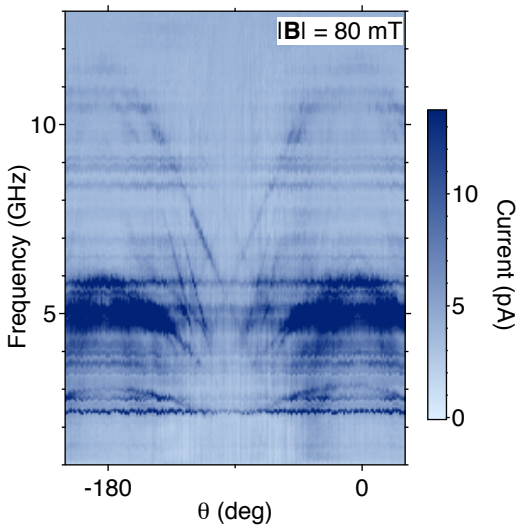

FIG. S1: **EDSR spectrum with magnetic field applied in yz plane**, This data was measured with the cryostat rotated by 90° compared to its orientation in the rest of the paper, so that the magnetic field was applied in the yz plane. As in Fig. 2 of the main text, $\theta = 0$ is defined as the z-axis. In these measurements, microwaves were applied continuously, with no pulses. The gate tuning was also slightly different than in Fig. 2. The key result is that the spectrum is symmetric about $\theta \approx 90°$, consistent with a qubit in the nanotube but unlikely to occur with a randomly oriented paramagnetic defect or adsorbed molecule. For this field orientation, EDSR can be mediated by the bend of the nanotube in the yz plane, or by a Rashba-like spin-orbit coupling[2].

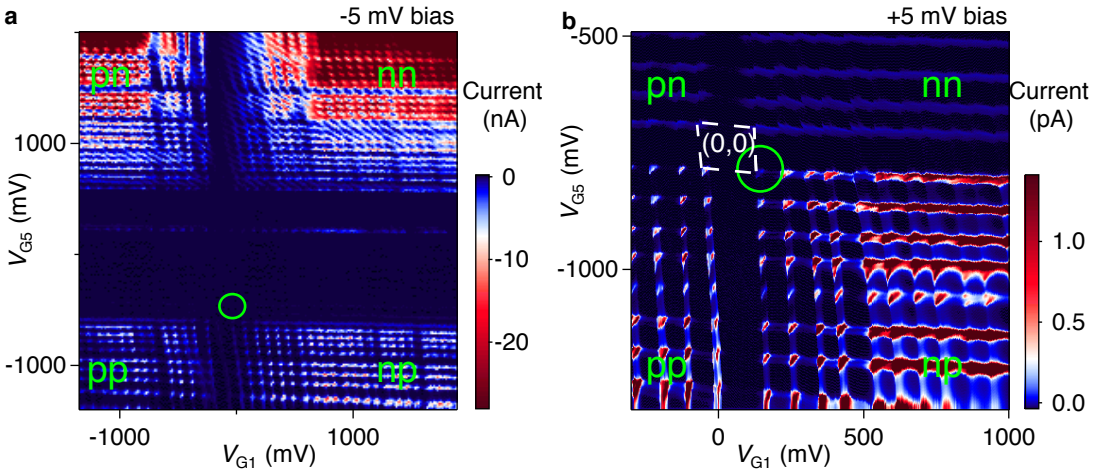

FIG. S2: **Large-range stability diagrams a**, Device current measured as a function of voltages on gates 1 and 5. The four double-dot regimes (nn, np, pp and pn) are accessed in the four high-current regions close to the corners of the diagram. When the chemical potential in one of the dots is tuned into the bandgap, current is suppressed; this is evident in the low-current cross that separates the high-current regions. **b** Zoom-in around the transition where EDSR was detected. The (0,0) double-dot configuration is evident as a particularly large cell in the honeycomb stability diagram (outlined in white). In both panels, the measured transition is circled in green.

B. Coulomb spectroscopy measurements

Extraction of the parallel g-factor $g_{||}$ from Coulomb blockade spectroscopy is shown in Fig. S3. The magnetic field dependence of the transition energies is measured[1] by sweeping across the cotunneling lines corresponding to the four single-dot transitions around (1,-1). The parameters we extract are similar to those measured at different transitions on a previous cooldown[1]. Taking an orbital g-factor of 21 and a Fermi velocity of 9×10^5 ms^{-1} gives[5] for the nanotube diameter 2.7 nm. The measured $g_{||}$ is approximately six times as large as deduced from the EDSR spectrum in Fig. 2 of the main text. The new type of measurement provided by EDSR therefore gives a significantly different result compared to transport (although meausured in a lower field range.) This discrepancy remains an open question for

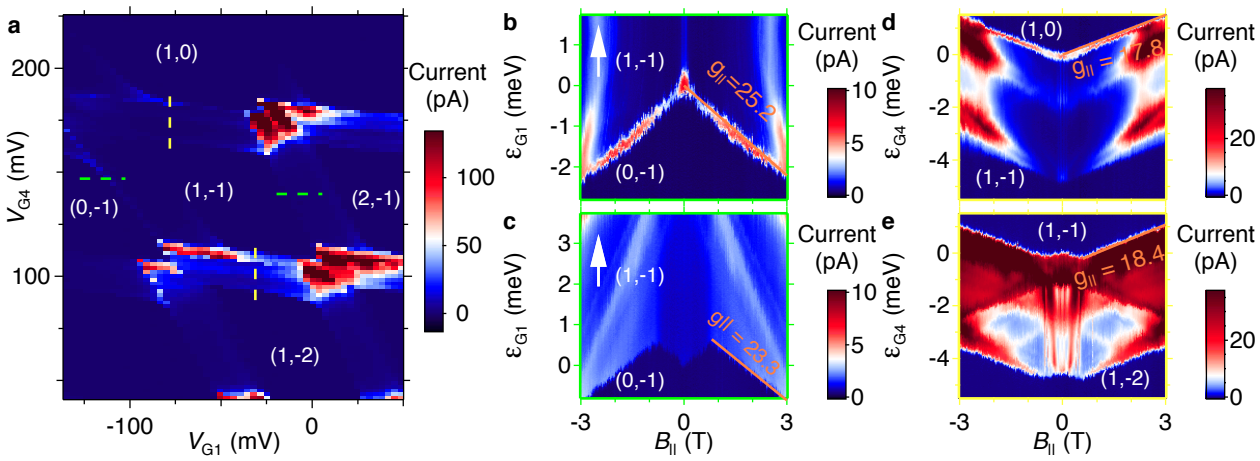

FIG. S3: **Coulomb blockade magnetospectroscopy a**, Stability diagram around (1,-1) configuration measured with 5 mV source-drain bias applied. **b-d**, Cuts along the marked lines in **a**, measured as a function of $B_{||}$. The corresponding single-dot transitions are: **b**, $0 \to 1$ (left dot), **c**, $1 \to 2$ (left dot), **d**, $0 \to -1$ (right dot), **e**, $-1 \to -2$ (right dot). The vertical axis is scaled from voltage V_G to energy ε_G. From the slope of the transition lines, the parallel g-factors can be extracted. The position of the kinks in c and d gives for the spin orbit energies $\Delta_{SO} = 1.0$ meV (electrons), 0.8 meV (holes).

future experiments.

From the sharpness of the kink at $\sim \pm 0.7$ T in Fig. S3c,e, we can place a bound on the valley-mixing parameter[6,7] $\Delta_{KK'} \leq 400$ μeV, consistent with $\Delta_{KK'} = 250$ μeV measured in a previous cooldown[1]. Combining the measured Δ_{SO} and $\Delta_{KK'}$ yields[8] a predicted $g_\perp \leq 0.8$, at least a factor of 2 smaller than derived from Fig. 2a of the main text.

III. SPIN RESONANCE DETECTION MECHANISM

The mechanism of EDSR detection using Pauli blockade is more complicated than in spin qubits, because a qubit flip by itself is not sufficient to break the blockade. For example, in a double quantum dot in spin blockade, with no valley quantum number, the blocked state $\uparrow\uparrow$ can be converted by a spin flip to $\uparrow\downarrow$, which overlaps with the non-blocked singlet state $(\uparrow\downarrow - \downarrow\uparrow)/\sqrt{2}$. However, in the situation of Fig. 1f in the main text, a qubit flip converts the initial state $\Downarrow\Downarrow^*$ to $\Uparrow\Downarrow^*$, which is still blocked. This differs from the situation for spin qubits[9–11], where Pauli blockade can be fully lifted by flipping a qubit state.

We believe the additional ingredient for detection is provided by disorder, which couples qubit states on the left and right dots. To see how, consider the particular example of magnetic field B along the x direction. The two single-dot Hamiltonians are then[12]:

$$H^\xi = \frac{\Delta_{SO}}{2}\sigma_3\tau_3 + \frac{1}{2}\{\Delta^\xi_{KK',1}\tau_1 + \Delta^\xi_{KK',2}\tau_2\} + \frac{g_s\mu_B}{2}B\sigma_x, \tag{1}$$

with the first term accounting for spin-orbit coupling, the second term for valley mixing, and the third term for Zeeman coupling. Here $\xi = \{L, R\}$ labels the two dots, Δ_{SO} is the spin-orbit splitting (known to be negative in this device[1]), and $\sigma_{1,2,3}$ and $\tau_{1,2,3}$ are Pauli matrices in spin and valley space respectively. Valley mixing due to random on-site disorder is parameterized by the coefficients $\Delta^\xi_{KK',1,2}$. Following Ref.[12], we define the quantities:

$$\Delta^\xi_{KK'} = |\Delta^\xi_{KK',1} - i\Delta^\xi_{KK',2}| \tag{2}$$

$$\varphi^\xi = \arg(\Delta^\xi_{KK',1} - i\Delta^\xi_{KK',2}). \tag{3}$$

For simplicity, the bend is neglected, and Δ_{SO} is assumed equal in both dots.

We now write out H^ξ explicitly (in the basis $\{K\uparrow, K'\downarrow, K\downarrow, K\uparrow\}$):

$$H^\xi = \begin{pmatrix} \Delta_{SO}/2 & 0 & \frac{g_s\mu_B}{2}B & \Delta^\xi_{KK'}e^{i\varphi^\xi} \\ 0 & \Delta_{SO}/2 & \Delta^\xi_{KK'}e^{-i\varphi^\xi} & \frac{g_s\mu_B}{2}B \\ \frac{g_s\mu_B}{2}B & \Delta^\xi_{KK'}e^{i\varphi^\xi} & -\Delta_{SO}/2 & 0 \\ \Delta^\xi_{KK'}e^{-i\varphi^\xi} & \frac{g_s\mu_B}{2}B & 0 & -\Delta_{SO}/2 \end{pmatrix}. \tag{4}$$

The four qubit states are the eigenstates of this Hamiltonian, written here without normalization:

$$|\Uparrow^*_\xi\rangle = \begin{pmatrix} e^{i\varphi^\xi} \\ 1 \\ -\frac{\Delta_{SO}/2-\sqrt{\Delta_{SO}^2/4+(g_s\mu_B B/2+\Delta^\xi_{KK'})^2}}{g_s\mu_B B/2+\Delta^\xi_{KK'}} e^{i\varphi^\xi} \\ -\frac{\Delta_{SO}/2-\sqrt{\Delta_{SO}^2/4+(g_s\mu_B B/2+\Delta^\xi_{KK'})^2}}{g_s\mu_B B/2+\Delta^\xi_{KK'}} \end{pmatrix}, \quad |\Downarrow^*_\xi\rangle = \begin{pmatrix} e^{i\varphi^\xi} \\ -1 \\ -\frac{\Delta_{SO}/2-\sqrt{\Delta_{SO}^2/4+(g_s\mu_B B/2-\Delta^\xi_{KK'})^2}}{g_s\mu_B B/2-\Delta^\xi_{KK'}} e^{i\varphi^\xi} \\ \frac{\Delta_{SO}/2-\sqrt{\Delta_{SO}^2/4+(g_s\mu_B B/2-\Delta^\xi_{KK'})^2}}{g_s\mu_B B/2-\Delta^\xi_{KK'}} \end{pmatrix},$$

$$|\Uparrow_\xi\rangle = \begin{pmatrix} \frac{g_s\mu_B B/2-|\Delta^\xi_{KK'}|}{\Delta_{SO}/2+\sqrt{\Delta_{SO}^2/4+(g_s\mu_B B/2-\Delta^\xi_{KK'})^2}} e^{i\varphi^\xi} \\ -\frac{g_s\mu_B B/2-\Delta^\xi_{KK'}}{\Delta_{SO}/2+\sqrt{\Delta_{SO}^2/4+(g_s\mu_B B/2-\Delta^\xi_{KK'})^2}} \\ -e^{i\varphi^\xi} \\ 1 \end{pmatrix}, \quad |\Downarrow_\xi\rangle = \begin{pmatrix} -\frac{g_s\mu_B B/2+|\Delta^\xi_{KK'}|}{\Delta_{SO}/2+\sqrt{\Delta_{SO}^2/4+(g_s\mu_B B/2+\Delta^\xi_{KK'})^2}} e^{i\varphi^\xi} \\ -\frac{g_s\mu_B B/2+\Delta^\xi_{KK'}}{\Delta_{SO}/2+\sqrt{\Delta_{SO}^2/4+(g_s\mu_B B/2+\Delta^\xi_{KK'})^2}} \\ e^{i\varphi^\xi} \\ 1 \end{pmatrix}. \tag{5}$$

Decay of a nominally blocked two-qubit state occurs because of mixing between an occupied state on the left and an unoccupied state on the right. This happens because of the asymmetry of $\Delta^\xi_{KK'}$ and ϕ^ξ, between left and right dots set by the random disorder potential. In the case shown in Fig. 1 of the main text, decay of the state $\Uparrow_L\Downarrow^*_R$ to $\Uparrow^*_R\Downarrow^*_R$ is governed by the matrix element $\langle\Uparrow_L | \Uparrow^*_R\rangle$, while that of $\Downarrow_L\Downarrow^*_R$ to $\Uparrow^*_R\Downarrow^*_R$ is governed by the matrix element $\langle\Downarrow_L | \Uparrow^*_R\rangle$. These two matrix elements are in general unequal. To show this, we calculate them from Equation (5) to lowest order in B and $\Delta^\xi_{KK'}$:

$$\langle\Uparrow_L | \Uparrow^*_R\rangle = i\frac{e^{i(\varphi^R-\varphi^L)/2}}{\Delta_{SO}}(\Delta^R_{KK'}-\Delta^L_{KK'})\sin\frac{\varphi^R-\varphi^L}{2} \tag{6}$$

$$\langle\Downarrow_L | \Uparrow^*_R\rangle = \frac{e^{i(\varphi^R-\varphi^L)/2}}{\Delta_{SO}}(\Delta^R_{KK'}-\Delta^L_{KK'})\cos\frac{\varphi^R-\varphi^L}{2}. \tag{7}$$

Our measurements do not allow us to determine which of these matrix elements has the larger magnitude. In the main text, we assume $|\sin((\varphi^R-\varphi^L)/2)| > |\cos((\varphi^R-\varphi^L)/2)|$, so that the $\Uparrow$ state decays faster than $\Downarrow$. In either case, so long as $|\sin((\varphi^R-\varphi^L)/2)| \neq |\cos((\varphi^R-\varphi^L)/2)|$, one qubit state will decay faster than the other, leading to a measurable current on resonance, as observed.

IV. FITS TO RABI DATA

To fit the data shown in Fig. 3a of the main text, we assume dephasing due to a slowly varying frequency detuning for each qubit, for example due to hyperfine fluctuations[13,14]. During each repetition of the pulse cycle of Fig. 1f, these detunings are assumed constant, but over many repetitions, the measured current $I(t_{burst})$ is proportional to the qubit flip probability averaged over all detuning configurations. This situation was previously considered in Ref.[14], where an approximate expression for $I(t_{burst})$ was derived in the limit $t_{burst} \gg T_2^*$. To calculate the fitting functions in Fig. 3a, we perform a more general analysis without this assumption.

We assume that only one qubit is close to resonance. Then for given angular frequency detuning $\delta\omega$ and Rabi angular frequency Ω_R, the flip probability due to coherent driving for time t_{burst} is

$$P_{flip}(t_{burst},\delta\omega,\Omega_R) = \frac{1}{2}\left[1+\frac{\delta\omega^2}{\Omega_R^2+\delta\omega^2}+\frac{\Omega_R^2}{\Omega_R^2+\delta\omega^2}\cos\left(\sqrt{\Omega_R^2+\delta\omega^2}\ t_{burst}\right)\right]. \tag{8}$$

The average qubit flip probability over all detuning configurations is then[13,14]

$$\overline{P}_{flip}(t_{burst},\Omega_R) = \int_{-\infty}^{\infty} P_{flip}(t_{burst},\delta\omega,\Omega_R)D(\delta\omega)d(\delta\omega), \tag{9}$$

where $D(\delta\omega) = \frac{1}{\sqrt{2\pi}\sigma} e^{-\frac{\delta\omega^2}{2\sigma^2}}$ is the detuning distribution function and $\sigma = \sqrt{2}/T_2^*$. The current in Fig. 3a is proportional to this spin-flip probability, together with an offset I_0 due to other leakage mechanisms and a small term due to incoherent photon-assisted tunneling that is proportional to $t_{\rm burst}$:

$$I(t_{\rm burst}) = I_0 + a\overline{P}_{\rm flip}(t_{\rm burst}, \Omega_{\rm R}) + bt_{\rm burst}, \tag{10}$$

The curves in Fig. 3a are obtained from Equation (10), with I_0, $\Omega_{\rm R}$, and the proportionality constants a and b taken as fit parameters. The calculated fidelity[15] of a π-pulse in this model is found to be 90% for the highest drive power in Fig. 3b.

To fully account for the data of Reference[14], the authors found it necessary to include terms in Equation (10) arising from combined spin-flips in both quantum dots, as expected because both spins had the same resonance frequency. For the fits in Fig. 3a, this leads to worse agreement with the data (not shown) suggesting that only one qubit is close to resonance. This implies that $|\mathbf{B}^{\rm eff}|$ differs between the two dots, as expected for an asymmetrically bent nanotube.

V. COMPARISON OF RABI FREQUENCY WITH THEORY

We compare the measured Rabi frequencies in Fig. 3b of the main text with theoretical expectations based on Equation (10) of Ref.[8], which for $\theta = 0$ predicts for the effective EDSR driving field $B_1^{\rm eff}$:

$$\frac{B_1^{\rm eff}}{B^{\rm eff}} = \frac{\delta\langle z\rangle}{r}\frac{g_{||} - g_\perp}{2g_\perp}, \tag{11}$$

where $\delta\langle z\rangle$ is the displacement of the dot in response to the driving voltage and r is the bend radius. For a parabolic confinement potential, the displacement of a single quantum dot is given by $\delta\langle z\rangle = eEL^2/\hbar\omega_0$, where L is the confinement length, E the electric field, and $\hbar\omega_0$ is the confinement level spacing.

For the strongest excitation in Fig. 3b, we estimate $E \approx \sqrt{2}\alpha V_{\rm ac}/2L \approx 4.0\times10^4$ Vm^{-1}, where $\alpha \approx 0.16$ is the gate lever arm, $V_{\rm ac} \approx 35$ mV is the rms microwave amplitude, and $L \approx 100$ nm from the gate geometry. In a previous cooldown we measured $\hbar\omega_0 \approx 3$ meV, giving $\delta\langle z\rangle \approx 130$ nm. Taking $g_\perp = 1.8$ and $g_{||} = 3.0$ from the spectra of Fig. 2, and $r \approx 600$ nm from the geometry gives $B^{\rm eff} = g_\perp|\mathbf{B}|/2 \approx 13.5$ mT and $B_1^{\rm eff} \approx 1.0$ mT. The expected Rabi frequency for this drive amplitude is then $f_{\rm R} = 2\mu_{\rm B}B_1^{\rm eff}/2 \approx 28$ MHz, in fair agreement with the measured $f_{\rm R} = 85$ MHz given the uncertainties involved.

VI. SOURCES OF DECOHERENCE

Several physical processes could contribute to dephasing (limiting T_2^*) and decoherence (limiting $T_{\rm echo}$) in this device. We consider each of them in turn.

A. Cotunneling

Although the device is configured in Coulomb blockade during the manipulation pulse, an electron could nevertheless be replaced from the leads via cotunneling, randomizing its spin. This would limit both $T_{\rm echo}$ and the relaxation time T_1. We exclude this possibility by showing that our data is inconsistent with such a short T_1. Figure S4a compares Rabi oscillations with microwaves applied close to the end of the manipulation pulse, and with the microwaves applied earlier so that the device waits for an additional 400 ns in Coulomb blockade[11]. Within the experimental error, the traces are identical, showing that $T_1 \gg 400$ ns. In Fig. S4b, the Rabi oscillation amplitude is plotted as a function of waiting time $t_{\rm wait}$ in Coulomb blockade, together with fits of the form $e^{-t_{\rm wait}/T_1}$. A least-squares fit gives $T_1 = 2.5$ μs. (The data are almost equally consistent with $T_1 = \infty$.) However, taking $T_1 = T_{\rm echo}$, as necessary to explain the decoherence by cotunneling, predicts a decay of the Rabi amplitude that is clearly inconsistent with the data. Furthermore, if cotunneling is a source of decoherence, $T_{\rm echo}$ would be expected to depend on the detuning during the manipulation pulse, which is in contrast with what we observe (not shown).

B. Paramagnetic defects

Randomly distributed paramagnetic defects in the atomic layer deposited Al_2O_3 substrate can cause decoherence by giving rise to a fluctuating magnetic field at the nanotube. In this section, we estimate the magnitude of this

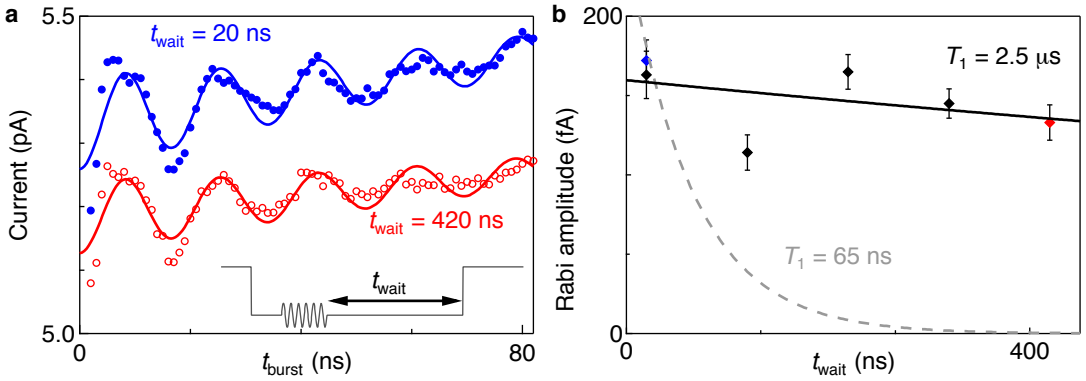

FIG. S4: **Measuring the relaxation time** T_1 **a**, Rabi oscillations measured with the microwave burst applied close to the beginning (red) and close to the end (blue) of the manipulation pulse. The two traces are almost identical, showing that negligible relaxation occurs during $t_{\rm wait}$. **b** Rabi oscillation amplitude as a function of $t_{\rm wait}$, with error bars set by the uncertainty of the fits to Eqn. 10. A least-squares fit (solid line) to the Rabi amplitude of the form $\propto e^{-t_{\rm wait}/T_1}$ yields $T_1 = 2.5$ μs. The data are clearly inconsistent with $T_1 = 65$ ns.

field. We consider the field as generated by a large number of classical magnetic moments $\mathbf{m}_i$ distributed over random locations $\mathbf{r}_i$ in the substrate (Fig. S5a). The field at location $\mathbf{r}$ due to a single moment is[16]:

$$\mathbf{B}_i(\mathbf{r}) = \frac{\mu_0}{4\pi}\left[\frac{3(\mathbf{r}-\mathbf{r_i})(\mathbf{r}-\mathbf{r_i})\cdot\mathbf{m_i}}{|\mathbf{r}-\mathbf{r}_i|^5} - \frac{\mathbf{m}_i}{|\mathbf{r}-\mathbf{r}_i|^3}\right]. \tag{12}$$

Since an electron in a quantum dot traverses the dot many times within one Larmor precession period, the qubit experiences the average of this field over the length of the dot,

$$\overline{\mathbf{B}}_i = \frac{1}{L}\int_{-L/2}^{L/2} dz\ \mathbf{B}_i(\mathbf{r}), \tag{13}$$

where $\mathbf{r} = (0, 0, z)$. The total field is the sum of this quantity over all individual magnetic moments, $\overline{\mathbf{B}} = \sum_i \overline{\mathbf{B}}_i$.

We evaluate this summation numerically for four different defect densities over an ensemble of sixteen defect configurations at each density. Each configuration consists of randomly chosen defect locations $\mathbf{r}_i$ (over a 3 nm × 6 nm × 210 nm volume, excluding defect sites within one nanotube radius $r_0 = 1.4$ nm of the z-axis) and random orientations of $\mathbf{m}_i$. The magnitude of each moment is fixed at the value appropriate for spin 1/2, $|\mathbf{m}_i| = \sqrt{\frac{1}{2}(1+\frac{1}{2})}\mu_{\rm B}$.

The simulated results are plotted in Fig. S5b for various defect densities. It is seen that at the highest densities simulated, which correspond to one magnetic moment per atomic site in the substrate, the rms components of $\overline{\mathbf{B}}$ are all below 1 mT. Taking $g = 2$, this corresponds to a dephasing time $T_2^* = \sqrt{2}\hbar/g\mu_{\rm B}B^{\rm rms}_{\rm x,y,z} > 8$ ns. Since this defect density is unrealistic, we conclude that neither T_2^* nor $T_{\rm echo}$ are limited by this mechanism. (To limit $T_{\rm echo}$, the defect density would have to be at least one per 30 atomic sites, which we also consider unrealistic.)

C. Hyperfine coupling

Hyperfine coupling is the major source of decoherence in III-V spin qubits[9–11,17,18] and has been previously measured for an isotopically purified ^{13}C nanotube quantum dot[19]. An upper limit of spin $T_2^* \leq 3.2$ ns was obtained, consistent with hyperfine coupling constant $A \sim 100$ μeV measured by analyzing the leakage current in spin blockade[20]. In that device, with similar dimensions to ours, the number of nuclei in the quantum dot was estimated as $N \approx 7 \times 10^4$, of which 99% were ^{13}C. In our device, taking a lithographic dot length of $L = 200$ nm (approximately consistent with the ~ 4 meV measured level spacing) and the nanotube diameter of 2.7 nm gives the same value for N, of which 1.1 % are ^{13}C. Since T_2^* scales as $\sqrt{N/p}$, where p is the isotopic fraction of ^{13}C, this predicts $T_2^* \leq 30$ ns, consistent with our results and suggesting that this may be the main source of inhomogeneous dephasing in our experiment. As pointed out in Ref.[20], this value of A is surprisingly high compared with theoretical expectations and NMR measurements of fullerenes and nanotubes.[21–23]

Hyperfine interaction also limits $T_{\rm echo}$ because of nuclear spin diffusion during the manipulation sequence[24]. However, the short $T_{\rm echo}$ we measure compared to GaAs would imply substantially faster spin diffusion, which is surprising

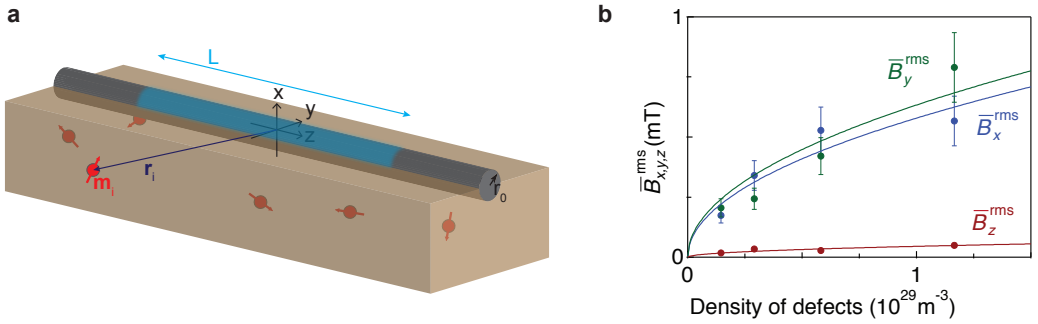

FIG. S5: **Calculation of dephasing by paramagnetic defects a**, Randomly distributed defects with magnetic moments $\mathbf{m}_i$ located at positions $\mathbf{r}_i$ create a magnetic field at the nanotube. An electron in the quantum dot experiences the average field over the confinement length L. The variance of this field over different configurations of $\{\mathbf{m}_i\}$ leads to decoherence. **b** Numerical simulation of $\overline{\mathbf{B}}$. The rms components of $\overline{\mathbf{B}}$ are plotted versus defect density ρ, with standard errors over the simulated configurations marked. Fits (lines) of the form $\overline{B}^{\rm rms}_{\rm x,y,z} \propto \rho^{1/2}$ agree well with the simulation. To give the measured dephasing rate, at least one component $\overline{B}^{\rm rms}_{\rm x,y,z}$ would have to be ~ 1 mT. Even at the highest density simulated, which corresponds to one electron spin per substrate atom, this field is not obtained. This mechanism therefore does not set the measured T_2^*, and probably not $T_{\rm echo}$ either.

given the one-dimensional character and larger nuclear spin spacing in a nanotube. A further argument against this interpretation comes from the exponent $\alpha = 1.3 \pm 0.2$ measured in Fig. 4b of the main text; nuclear spin diffusion is expected[24] to give $3 \leq \alpha \leq 4$. Finally, in III-V systems where hyperfine decoherence is believed to dominate, a Carr-Purcell burst sequence leads to an improvement in coherence time, which we did not observe[11,18]. We therefore consider it unlikely that hyperfine coupling limits $T_{\rm echo}$ in our experiment.

D. Charge noise

Charge noise can contribute to decoherence by causing jitter of the gate detuning. As seen from Fig. 2d of the main text, this leads to a random frequency shift which causes dephasing and decoherence. To give the decay curve in Fig. 4a of the main text, the root-mean-square frequency jitter would have to be $\Delta f = \sqrt{2}/T_2^* = 180$ MHz. From Fig. 2d, this would correspond to a detuning jitter of ~ 0.6 meV, corresponding to a gate voltage jitter ~ 3.6 mV. Such a jitter is not inconsistent with our data; the narrowest features in a stability diagram such as Fig. 1e of the main text have approximately this width, although they could equally be tunnel-broadened. Although we consider it unlikely that so much electrical noise could be present in our setup, we cannot exclude the possibility of equivalent noise arising from charge switchers in the substrate, or from mechanical motion of the nanotube. Charge noise should therefore be considered as a possible source of dephasing.

The echo pulse sequence extends coherence by cancelling out slowly varying noise, but high-frequency jitter cannot be echoed away. The measured $T_{\rm echo}$ can be accounted for by jitter having a white-noise power spectrum[24] with magnitude $S_0^f = 1/2T_{\rm echo}$. This corresponds to detuning noise of $\epsilon_{\rm noise} \approx 10$ neV$/\sqrt{\rm Hz}$. Assuming a cutoff of the white-noise spectrum at 100 MHz, consistent with the measured decay, the root-mean-square detuning jitter would be ~ 0.1 meV, corresponding to a gate jitter ~ 0.6 mV, which is also consistent with the stability diagram. Of the mechanisms we have considered, we suggest that this is most plausible as the main process that limits $T_{\rm echo}$, although data presented in the next section shows that other effects also contribute.

VII. MEASUREMENTS ON A LOWER RESONANCE LINE

In the main paper, we focused on measuring the highest-frequency line because it gave the clearest Rabi oscillations. However, we were also able to perform qubit operations using a lower line (Fig. S6). The spectrum of this line is shown in Fig. S6a,b. Interestingly, the resonance frequency depends approximately six times less strongly on detuning than the lines shown in Fig. 2d of the main text. This might therefore be expected to make the qubit less sensitive to charge noise. Figures S6 c and d show the results of dephasing and coherence time measurements similar to Fig. 4 of the main text. As can be seen, the decay of qubit interference fringes is similar to the results in the main text; the corresponding times are $T_2^* = 8 \pm 1$ ns (the same as in the main text), and $T_{\rm echo} = 97 \pm 15$ ns (a factor 1.5 ± 0.3 longer). With perfect pulses and in the absence of other decoherence sources, a sixfold reduction in coupling to low-frequency charge noise should lead to[24] a sixfold increase in T_2^* and a factor $6^{-2/\alpha} \approx 16$ increase in $T_{\rm echo}$. This data therefore

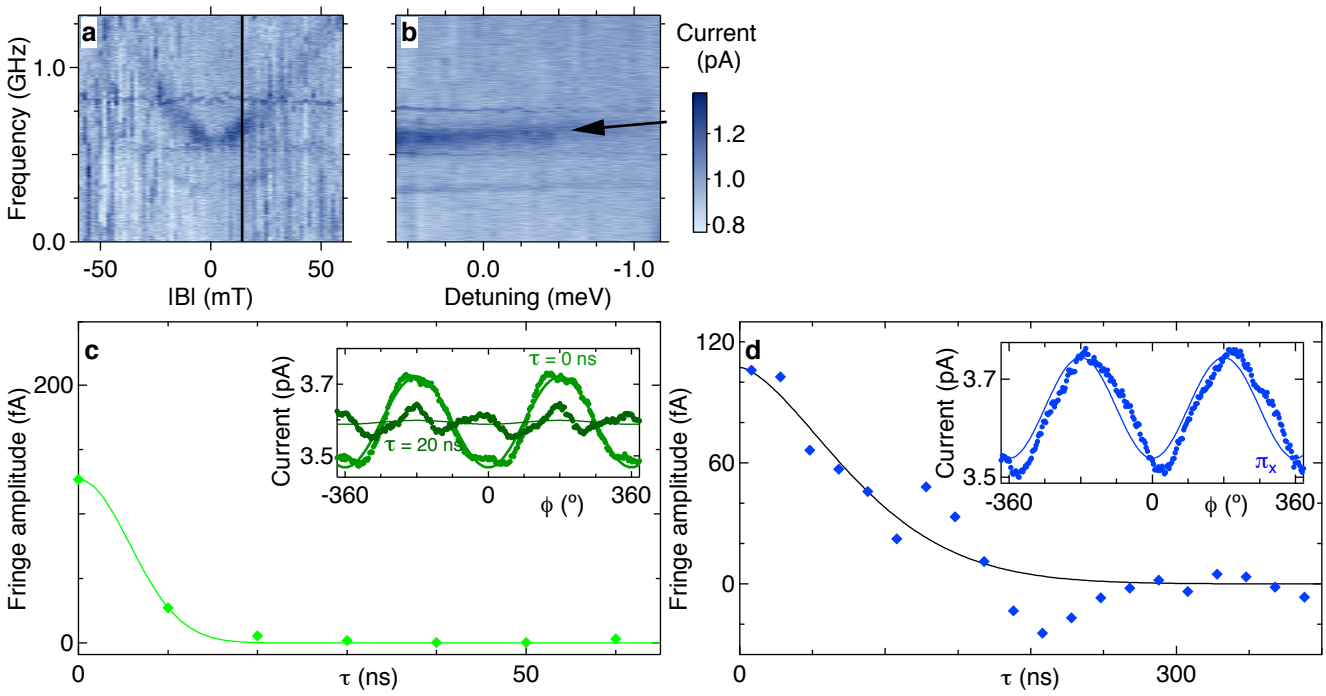

FIG. S6: **Measurements on a lower line a**, Spin resonance spectrum below 1.3 GHz as a function of magnetic field with $\theta = 0$. **b**, Spectrum as a function of detuning at 14 mT. The slope is approximately six times less than in Fig. 2d of the main text, and of the opposite sign. **c**, Ramsey and **d**, echo measurements of the strongest line in panel b (marked with arrow), similar to the measurements in Fig. 4. The corresponding qubit lifetimes are $T_2^* = 8 \pm 1$ ns, and $T_{\rm echo} = 97 \pm 15$ ns.

implies that T_2^* is not sensitive to charge noise (as would be expected if it is limited by hyperfine coupling), and that $T_{\rm echo}$ is sensitive to charge noise on the detuning axis but is also limited by some unknown decoherence mechanism, at least for this resonance line. One possibility is that the qubit state couples to electric fields that are not simply equivalent to detuning noise, for example to a change in interdot tunnel coupling. The sensitivity to electrical noise may therefore be larger than expected from Fig. S6b alone.

[1] Pei, F., Laird, E. A., Steele, G. A. & Kouwenhoven, L. P. Valley-spin blockade and spin resonance in carbon nanotubes. *Nat Nanotechnol* **7**, 630 (2012).

[2] Klinovaja, J., Schmidt, M. J., Braunecker, B. & Loss, D. Carbon nanotubes in electric and magnetic fields. *Phys Rev B* **84**, 085452 (2011).

[3] Minot, E. D. et al. Tuning carbon nanotube band gaps with strain. *Phys Rev Lett* **90**, 156401 (2003).

[4] Deshpande, V. V. et al. Mott insulating state in ultraclean carbon nanotubes. *Science* **323**, 106–110 (2009).

[5] Minot, E. D., Yaish, Y., Sazonova, V. & McEuen, P. L. Determination of electron orbital magnetic moments in carbon nanotubes. *Nature* **428**, 536–539 (2004).

[6] Kuemmeth, F., Ilani, S., Ralph, D. C. & McEuen, P. L. Coupling of spin and orbital motion of electrons in carbon nanotubes. *Nature* **452**, 448–452 (2008).

[7] Jespersen, T. S. et al. Gate-dependent spin–orbit coupling in multielectron carbon nanotubes. *Nat Phys* **7**, 348–353 (2011).

[8] Flensberg, K. & Marcus, C. M. Bends in nanotubes allow electric spin control and coupling. *Phys Rev B* **81**, 195418 (2010).

[9] Koppens, F. H. L. et al. Driven coherent oscillations of a single electron spin in a quantum dot. *Nature* **442**, 766–771 (2006).

[10] Nowack, K. C., Koppens, F. H. L., Nazarov, Y. V. & Vandersypen, L. M. K. Coherent control of a single electron spin with electric fields. *Science* **318**, 1430–1433 (2007).

[11] Nadj-Perge, S., Frolov, S. M., Bakkers, E. P. A. M. & Kouwenhoven, L. P. Spin-orbit qubit in a semiconductor nanowire. *Nature* **468**, 1084–1087 (2010).

[12] Reynoso, A. A. & Flensberg, K. Dephasing and hyperfine interaction in carbon nanotubes double quantum dots: disordered case. *Phys Rev B* **85**, 195441 (2012).

[13] Coish, W. A. & Loss, D. Singlet-triplet decoherence due to nuclear spins in a double quantum dot. *Phys Rev B* **72**, 12 (2005).

[14] Koppens, F. H. L., Nowack, K. C. & Vandersypen, L. M. K. Spin echo of a single electron spin in a quantum dot. *Phys Rev*

Lett **100**, 4 (2008).
[15] Koppens, F. H. L. et al. Universal phase shift and nonexponential decay of driven single-spin oscillations. *Phys Rev Lett* **99**, 106803 (2007).
[16] Jackson. *Classical electrodynamics* (John Wiley and Sons, 1999), third edition.
[17] Petta, J. R. et al. Coherent manipulation of coupled electron spins in semiconductor quantum dots. *Science* **309**, 2180–2184 (2005).
[18] Bluhm, H. et al. Dephasing time of GaAs electron-spin qubits coupled to a nuclear bath exceeding 200 μs. *Nature Physics* **7**, 109–113 (2011).
[19] Churchill, H. O. H. et al. Relaxation and dephasing in a two-electron ^{13}C nanotube double quantum dot. *Phys Rev Lett* **102**, 166802 (2009).
[20] Churchill, H. O. H. et al. Electron–nuclear interaction in ^{13}C nanotube double quantum dots. *Nature Physics* **5**, 321–326 (2009).
[21] Pennington, C. H. & Stenger, V. A. Nuclear magnetic resonance of C_{60} and fulleride superconductors. *Rev Mod Phys* **68**, 855 (1996).
[22] Yazyev, O. V. Hyperfine interactions in graphene and related carbon nanostructures. *Nano Lett* **8**, 1011–1015 (2008).
[23] Kiss, A. et al. Enhanced nmr relaxation of tomonaga-luttinger liquids and the magnitude of the carbon hyperfine coupling in single-wall carbon nanotubes. *Phys Rev Lett* **107**, 187204 (2011).
[24] Taylor, J. M. et al. Relaxation, dephasing, and quantum control of electron spins in double quantum dots. *Phys Rev B* **76**, 035315 (2007).